NIOLD Run 4 Report

M.K. Duncan[1], R. Ainsworth[2], A. Burov[2], N.Eddy[2], Y.K. Kim[1], and O. Mohsen[3]

[1]Department of Physics, The University of Chicago
[2]Fermi National Accelerator Laboratory
[3]Argonne National Laboratory

April 25, 2024

1 Introduction

A challenge faced by many particle accelerators is the challenge of maintaining high beam intensity. Often one desires to maximize the beam intensity of an accelerator, leading to a greater collision rate. Major factors limiting an accelerator's beam intensity include collective instabilities. Collective instabilities arise when a particle beam interacts with its surroundings to generate a wakefield. The wakefield then acts back on the beam and perturbs its motion. When the perturbations on the beam are enhanced by the wakefield, collective instabilities can be observed [9]. Collective instabilities not only reduce the beam intensity but produce losses, irradiate components, and produce additional negative effects.

In this experiment at the Integrable Optics Test Acceleartor (IOTA) at Fermilab, we aim to approach the grand challenge of beam intensity by studying beam stability. The effect we study to better understand beam stability is called Landau Damping. Landau Damping was originally derived for plasmas with a purely mathematical approach in 1946 by Lev Davidovich Landau [6]. The first experimental evidence of Landau Damping was observed 18 years later, in 1964 by Malmberg and Wharton [7].

In collisionless plasmas, as well as in particle accelerators, Landau Damping (LD) is the effect which damps collective oscillation modes and acts as a defense against collective instabilities. A physical interpretation of Landau Damping can be expressed as a mechanical model as follows.

Consider a model consisting of an infinite set of harmonic oscillators with a frequency distribution $G(\omega)$. The individual harmonic oscillators represent the individual particles in the accelerator, where the harmonic oscillator frequencies represent the particle's tunes. Consider an introduced external sinusodial force impacting the oscillators at a frequency Ω. Note that in this model all the oscillator frequencies are sufficiently close to one another and Ω lies within their range.

Now let us consider two individual oscillators in the group, one oscillating at frequency $\omega = \Omega$ and the other oscillating at frequency $\omega \neq \Omega$, though oscillating at a frequency close to Ω. The amplitude of the on-resonance oscillator grows linearly over time, as it resonates with the external force. The other particle increases in amplitude over some time, but loses synchronism with the external force at a later time and its amplitude decreases by being out of resonance. At some time t, only oscillators where $\omega - \Omega$ is sufficiently small will maintain the phase relation with the external force. The later the time, the smaller the bandwidth of synchronous oscillators with the external force. From this, the 'on resonance' oscillators are in phase with the external force and absorb energy from it, while their frequency bandwidth and number decreases with time. The net effect is an absorption of energy by the oscillators while the total energy of oscillations, both coherent and incoherent, remains constant. Therefore, the coherent instability, or external force, is damped by the oscillators [8]. A schematic representing the on-resonance and off-resonance particles, the external perturbation, and the particle's amplitudes over time can be seen below in Figure 1.

As in the mechanical model where Landau Damping depends on the spread of oscillator frequencies, Landau Damping in accelerators depends on the spread of particle betatron frequencies. Also as in the mechanical model, Landau Damping in accelerators works through the energy transfer between

This manuscript has been authored by Fermi Research Alliance, LLC under Contract No. DE-AC02-07CH11359 with the U.S. Department of Energy, Office of Science, Office of High Energy Physics.

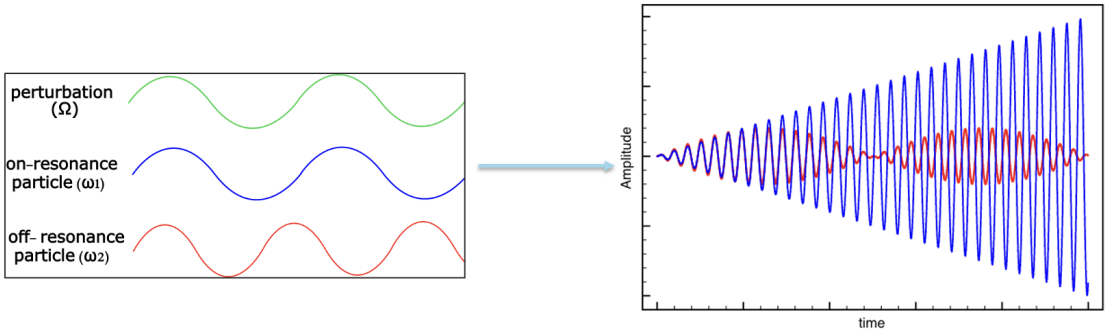

Figure 1: Left: Schematic representation of frequencies of the perturbation, on-resonance particle, and off-resonance particle. Right: Amplitude of particle oscillations over time. The on-resonance particle in blue gains amplitude constantly over time. The off-resonance particle in red begins gaining amplitude then goes out of phase with the perturbation [8].

coherent and incoherent oscillation modes, where it 'damps' the collective oscillation modes, stabilizing intense beams. A detailed knowledge of the strength of Landau Damping in particle accelerators is essential for predictions of beam stability. Studies and predictions of Landau Damping are often approached via Stability Diagram Theory.

Stability Diagram Theory for Landau Damping depends on the dispersion relation between the beam's coherent tune shift from an external excitation and the frequency of particles in the presence of Landau Damping, or the tune of the mode. The dispersion relation for a coherent vertical degree of freedom is shown in Eq. (1):

$$\Delta\omega = -1/\int \frac{J_y \partial F/\partial J_y}{\Omega + \delta\omega(J_x, J_y) + io}\, dJ_x dJ_y \tag{1}$$

Where $\Delta\omega$ is the coherent tune shift, Ω is the tune of the mode, J_y is the action in the y-plane, F is the bunch distribution function, $\delta\omega$ is the frequency shift of the oscillating particles, and io is a vanishingly small term introduced in derivation to avoid singularities. The derivation of this equation can be found in [2].

Given the coherent tune shift from an external source and using the dispersion relation in Eq. (1), one can find the resulting tune of the mode. To find the tune of the mode Ω, one would traditionally need to solve Eq. (1) for all $\Delta\omega$. Using this method, if one maps the plane of zero-imaginary Ω, $Im[\Omega] = 0$, onto the complex plane of the coherent tune shift $\Delta\omega$, then a threshold separating the stable and unstable states of the particle bunch can be mapped. This maps out a Stability Diagram (SD).

A schematic of a stability diagram where nonlinear focusing is fed in the y plane and the coherent tune shift is fed in the x plane can be seen below in Figure 2. The complex plane of $\Delta\omega$ is shown, where the blue curve is where $Im[\Omega] = 0$, defining the threshold between stable particle motion and unstable particle motion. Below the curve represents the region with stable motion and above the curve represents the region with unstable motion.

There are current techniques to measure stability diagrams for Landau Damping, though they have limitations. One main technique to measure stability diagrams is to measure the beam transfer function (BTF), which gives the frequency dependence of the beam's response to forced beam oscillations. Since the stability diagram goes as the inverse of the beam transfer function, stability diagrams can be measured this way, though this technique is somewhat limited. The major limitation is that this method does not test the strength of Landau Damping itself, but rather the beam transfer function, relying on assumptions behind the derivation of the dispersion relation of Eq. (1). These assumptions include that the synchrotron frequency is negligible, the betatron frequency is sufficiently small, the beam response to external excitations is linear, and that the coherent modes are uncoupled [1]. From the limitations of this technique, we investigate an alternative method to measure the strength of LD.

In the alternative method to measure the strength of Landau Damping, we revert the polarity of a transverse feedback in order to excite a coherent mode in the beam. This creates what is called an

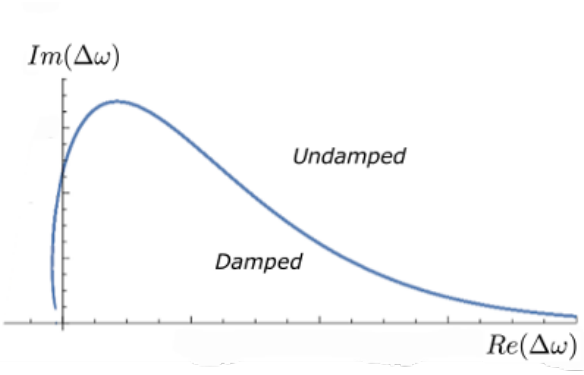

Figure 2: Stability Diagram, showing the threshold between stable and unstable particle motion.

antidamper. The antidamper produces a coupling impedance:

$$Z(\omega) \propto Ge^{i\phi}\delta(\omega) \tag{2}$$

Where G is the antidamper gain and ϕ is the antidamper phase. The $\delta(\omega)$ shows that the antidamper kicks the bunch as a whole. The details of the antidamper elements and operation will be discussed in the Experimental Setup section of this document.

The coupling impedance in Eq. (2) produces a coherent tune shift:

$$\Delta\omega \propto ge^{i\phi} \tag{3}$$

Where g is the growth rate in [1/turns] of the beam's centeroid position. The details of the beam's growth rate will be discussed in the Experimental Procedure section of this document.

From these properties of the antidamper, if one can independently change the gain and phase, then the antidamper is a source of controlled impedance. With this controlled source, different combinations of the phase and gain can be used to observe at which combinations does the beam initially become unstable, or in other words, when does the beam first have a growth rate above threshold.

A schematic to obtain a stability diagram with this method can be seen below in Figure 3. For different antidamper G and ϕ combinations, the growth rate of the beam's centeriod position is recorded. These G and ϕ combinations are represented in Fig. 3 by the arrow extending out to the stability curve. The G and ϕ combinations are changed until a growth rate is first observed, which is the growth rate used in Eq. (3) to map onto the stability diagram. An example of the turn-by-turn data for the growth rate can be seen in the top-right subfigure of Fig. 3. When the G and ϕ combinations are under the stability threshold, the beam's centeroid position is shown as the blue line in the subfigure. Once a G and ϕ combination produces an initial instability, the beams centeroid position has a growth rate, shown as the envelope of the red area in the subfigure. This growth rate is then used in Eq. (3) to map onto the complex $\Delta\omega$ plane at the red dot, which lies on the stability diagram.

This experiment with this measurement method was performed at the Integrable Optics Test Accelerator (IOTA) at Fermilab. IOTA is an easily re-configurable 40 m storage ring and is designed to run both electrons and protons, at energies of 150MeV and 2.5MeV, respectively. This experiment is dedicated for when electrons are circulating. Further details of the IOTA ring and the antidamper system will be presented in the Experimental Setup section of this document.

A proof-of-principle experiment of this stability diagram measurement method was performed previously at CERN, with results published in 2021 [1]. This proof-of-principle experiment was qualitatively successful and has inspired further research on this topic. As only three different phase data points were collected in the experiment, we aim to expand upon this work to quantitatively confirm this measurement method. This extension would be done by taking more phase measurements for a stability diagram. Additionally, as the authors of [1] inquire about the machine impedance's impact on the measured stability diagram, the IOTA experiment could investigate this, as the machine impedance of IOTA is much smaller than that of the LHC's. One additional investigation to be made with this experiment is to obtain the beam distribution function from the stability diagram, which has not been

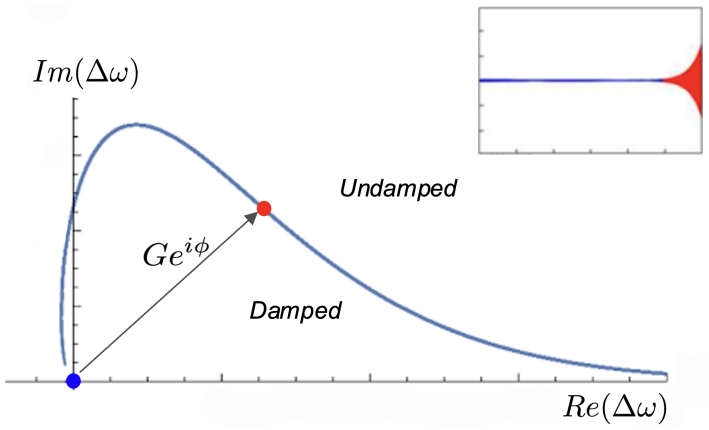

Figure 3: Stabilty Diagram, as it is obtained from an antidamper's gain G and phase ϕ.

done this way before. The theoretical procedure for finding the beam distribution function from the stability diagram can be found in [2].

2 Predictions

There are both analytical and simulation predictions for IOTA stability diagrams, aiding in understanding what we expect to see from measurements. It is important to note that during data collection the source of Landau Damping's nonlinear focusing was a string of octupoles, where these octupoles supplied Landau Damping in the horizontal plane (x). The excitation from the antidamper was alternatively fed in the vertical plane (y). The turn-by-turn data collected was also in the vertical plane. Therefore, the theoretical predictions and the simulations were analyzed under these conditions: the source of Landau Damping acting in the horizontal plane, the excitation fed in the vertical plane, and the beam response recorded in the vertical plane.

Under the conditions described, the normalized dispersion relation in Eq. (1) reduces to:

$$\Delta\omega = \left[\int dJ_x \frac{F_x(J_x)}{\Omega - J_x + io}\right]^{-1} \tag{4}$$

Where again, $\Delta\omega$ is the coherent tune shift, Ω is the tune of the mode, and J_x is the action in x. This simplification of the dispersion relation is further described in [2]. The corresponding normalized analytical stability diagram when the complex plane of $\Delta\omega$ is plotted for $Im[\Omega] = 0$ is shown in Figure 4a.

The stability diagram was also simulated for comparison. The simulation package used was Xsuite [5], which applies the Madx [3] IOTA lattice for simulations. The simulations were run with each octupole set to a current of 4A, high enough that the octupoles dominate the nonlinear focusing in the ring. The resulting simulated stability diagram, scaled by area to match the size of the normalized analytical stability diagram, can be seen in Figure 4b. From the analytical and simulation results, we expect to see a stability diagram resembling Figure 4b.

3 Experimental Setup

This experiment was performed when the IOTA ring was circulating electrons and an antidamper was used as the source of controlled impedance. To create the antidamper, a transverse feedback was used. Transverse feedbacks are often used in accelerators to preserve transverse emittances and damp particle beam oscillations. In this experiment, the polarity of the transverse feedback is reversed to coherently excite the beam rather than damp. The main experimental elements include a stripline kicker, two stripline BPMs, and a string of octupoles. The kicker and the BPMs create the antidamper system, where the octupoles supply the force for Landau Damping [4].

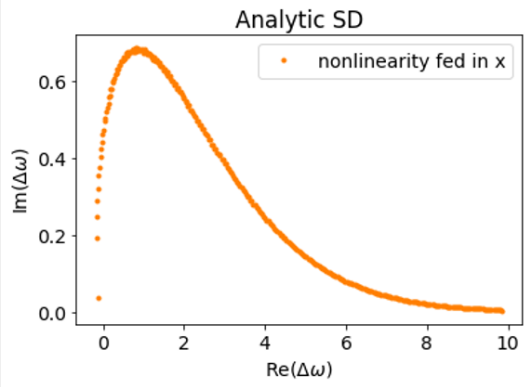

(a) Normalized analytical stability diagram when the nonlinearity is in the x plane and the excitation is in the y.

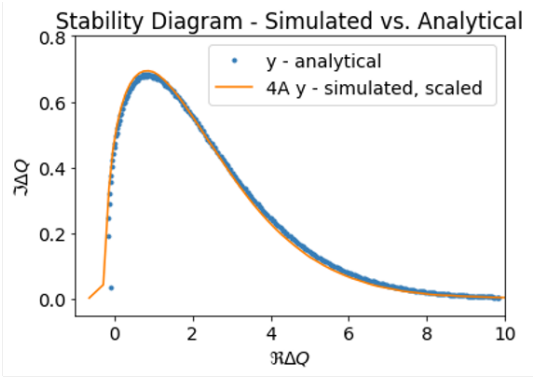

(b) Simulated and analytical stability diagrams together, the IOTA data is expected to follow these curves.

Figure 4

In the antidamper system, the stripline kicker is used to supply the excitation force to the beam and gives control to change the gain of the antidamper. The two stripline BPMs are located approximately 110° apart. This is so the two BPMs can be combined to create a virtual bpm, where the total phase advance from kicker to pickup can be altered, allowing for adjustment of the phase advance of the antidamper. A schematic of the antidamper system in the IOTA ring can be seen below in Figure 5

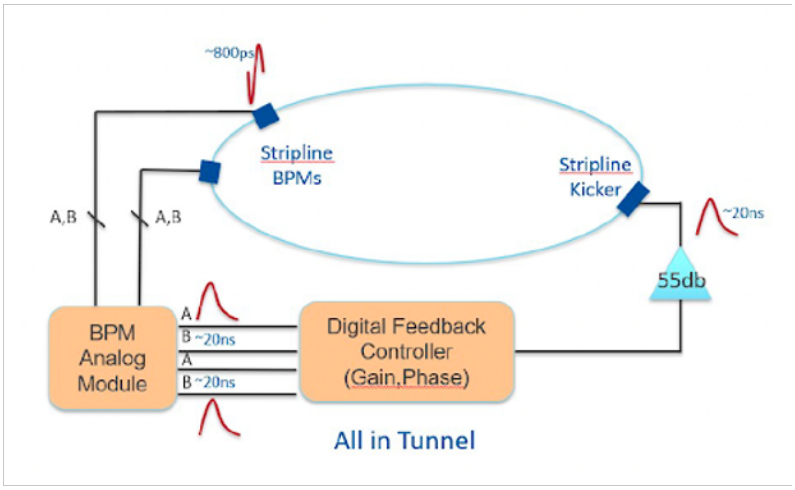

Figure 5: Schematic of antidamper elements in the IOTA ring [4].

The physical experimental elements in the tunnel can also be seen below in Figure 6. In Figure 6a, the antidamper kicker and BPMs are shown. Note that the kicker and BPMs are located within the quadrupole magnets which the arrows point to. In Figure 6b, the string of octupoles which act as the source of Landau Damping are shown. There are 9 octupoles in total. For the data presented in this report, all of the octupoles were set to the same current of 4A. This value is large enough to dominate the nonlinear focusing in the IOTA ring.

The locations of the experimental elements within the IOTA ring can be seen in Figure 7, where the region circled in blue is the location of the antidamper system and the region circled in red is the region of the octupole string. The use of these experimental elements will be described in the following section.

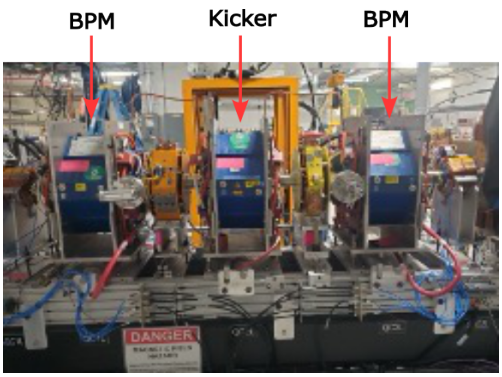

(a) Antidamper kicker and BPMs. They are located beneath the magnets.

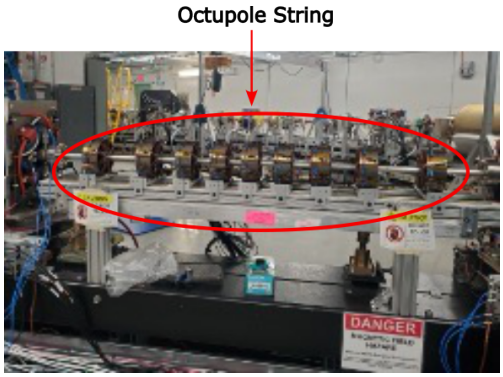

(b) String of octupoles which are the source of Landau Damping in the ring.

Figure 6

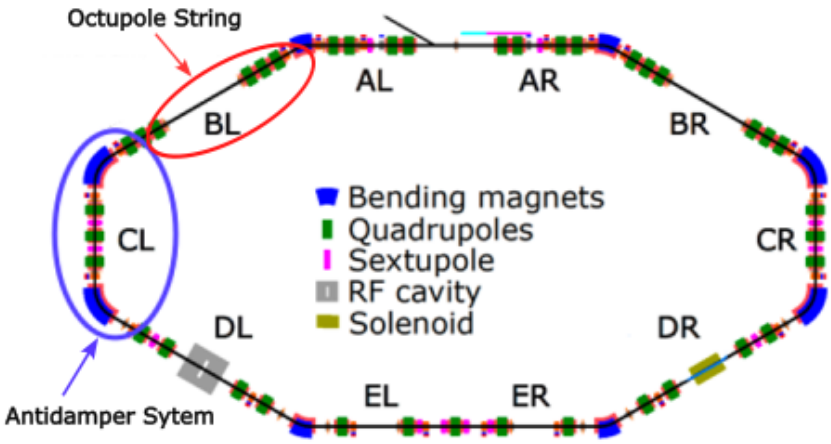

Figure 7: Schematic of the IOTA ring. The antidamper system is located in section CL and the octupole string is located in section BL.

4 Experimental Procedure

The data for Run 4 was collected in the Fall of 2023, specifically between 09/26/23 and 10/19/23. There were two shifts of commissioning. These shifts were followed by a few shifts where we were unable to collect beam size data due to the ACNET readback for the sync light system not working. While collecting data, we were unaware of the importance of the emittance variations in our analysis process and the lack of emittance data on these days made the data collected difficult to analyze. An example image of the beamsize data which we had difficulties collecting for the first few shifts is shown below in Figure 8. Once able to collect beamsize data, we had a few shifts with low octupole currents, where the effect of Landau Damping from the octupoles was less identifiable. On 10/19/23 the full set of data for high octupole currents was collected and is the data which we present in this document. It also important to note that the WCM data was not available in ACNET during data collection, though we were able to implement our own scope readback for the last few shifts. The WCM data is important because the bunch length impacts the system gain. A table listing out the dates and what data was collected for each is shown below in table 1.

To collect data, our procedure was to sweep through kicker gains and BPM coefficients. The change in BPM coefficients correspond directly to a change in the phase, which will be expanded on in the following section of this document. For each data collection, the phase of the antidamper (ϕ in Eq. (2)) was swept through. The phases were incremented by either 10° or 5° and ranged over a large phase

Table 1: NIOLD Run 4 Shifts

Date	Collection Notes
09/26/23	Commissioning
09/28/23	Commissioning
09/29/23	Data Collection - missing beamsize data
10/03/23	Data Collection - missing beamsize data
10/05/23	Data Collection - missing beamsize data
10/14/23	Data Collection - low octupole currents
10/17/23	Data Collection - low octupole currents
10/19/23	Data Collection - have all data

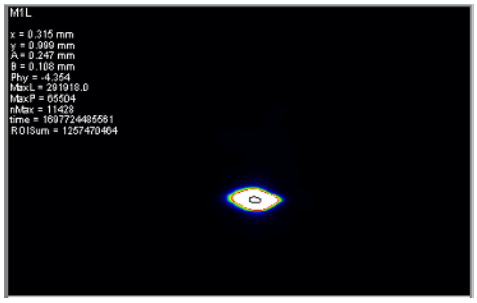

Figure 8: Example of camera M1L beamsize data.

sweep. Then, for each phase within the sweep, the kicker gain (G in Eq. (2)) was swept through. For the kicker gain, we performed a binary search to find the thresholds. The first growth rate for kicker gain per phase with an instability was the recorded growth rate for that phase. The growth rate g in [1/turns] and the phase in radians are the experimentally obtained values used in Eq. (3) to map out the stability diagram. An example of the beam's centroid position with a fitted growth rate from a phase and gain combination is shown below in Figure 9.

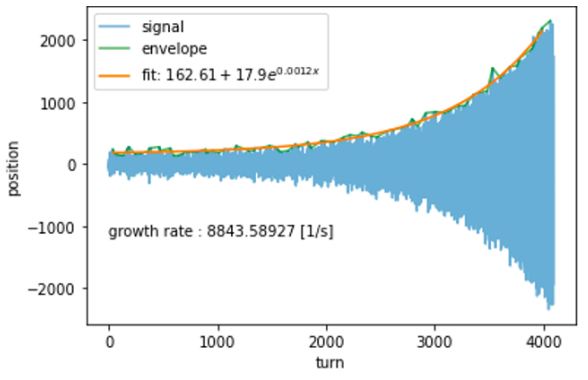

Figure 9: Example of beam centroid turn-by-turn data with an exponential fit to the envelope for growth rate.

Additionally, since the size of the stability diagram depends on the emittance, as presented in [2], the beamsize data was necessary to collect. The intensity data was also collected, as it also impacts the size of the stability diagram.

From this procedure, the major data elements collected include the phase from the pickup to kicker, the kicker gain, the growth rate at the first kicker per phase where instability is observed, the beamsize, and the intensity.

5 Data Analysis

To analyze the beam's growth rate per phase advance ϕ, the conversion between the bpm coefficients and the phase advance ϕ is performed.

In order to obtain the phase advance ϕ from BPM coefficients, one sweeps through the BPM coefficients and performs a Beam Transfer Function (BTF) for each of them. A BTF looks at the frequency dependence of the response to forced beam oscillations. This excitation is done at frequencies spanning the regions of the lower sideband and upper sideband of the revolution harmonic. The beam is kicked at the frequencies scanning these sidebands. The beam's amplitude response to the kick and the phase advance from kicker to virtual BPM are then recorded for each frequency. An example of a BTF can be seen below in Figure 10a. The phase corresponding to the maximum beam amplitude is the phase advance propagated for that particular BPM coefficient combination. The BPM coefficient combinations consisted of a sweep through BPM2 coefficients from -2.0 to 2.0 in steps of 0.1, while keeping BPM1 at 1.0. The phase advances for each of the BPM coefficient combinations for both the upper sideband and lower sideband are then used for calculation of the total phase advance from virtual pickup to kicker. An example of the upper and lower sideband phases can be seen in Figure 10b. Then to calculate the total phase advance the following equation is used:

$$((\theta_{usb} - \theta_{lsb}) + 180)/2 = \phi \tag{5}$$

Where θ_{usb} is the phase advance of the upper sideband, θ_{lsb} is the phase advance of the lower sideband, and ϕ is the total phase advance. Therefore, for each BPM coefficient combination there is a mapping to a phase value. An example of this mapping can be seen below in Figure 10c. So, for each BPM combination used in data collection, a phase advance is obtained, giving the phase needed to compute $\Delta\omega$ from Eq. (3).

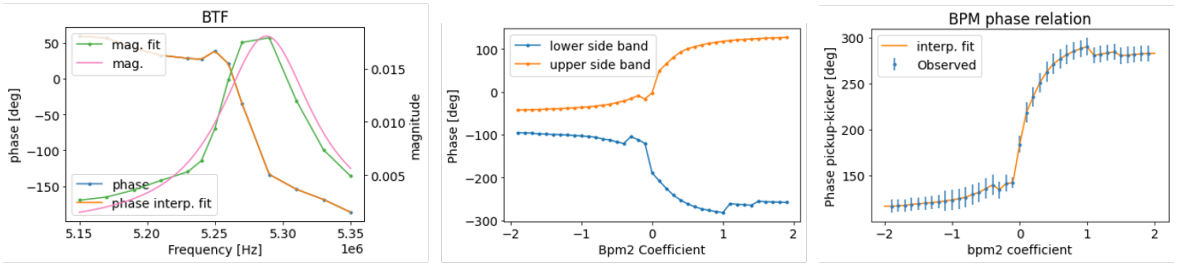

(a) Example of a BTF. The phase at the maximum amplitude response is the phase advance.

(b) Example of upper and lower sideband phases per BPM2 coefficient.

(c) Example of final BPM2 coefficient to total phase advance relationship.

Figure 10

Since the BTF ranges available do not cover the full phase map, BTF data was taken at different turn delays. The turn delays are described by additional turns in the ring before the phase data was collected. Each additional turn advanced the phase by approximately 60°. This allowed us to cover more phases for the stability diagrams. The data that is presented here is specifically for when there are no additional turn advances before phase data collection and when there were two turn advances before phase data collection.

The next analysis step is to obtain the growth rate for each phase advance, particularly to determine at what kicker gain is a growth in the beam centroid position observed. An example of the turn-by-turn centroid data at a kicker gain right before the first growth and a kicker gain right after the first growth can be seen below in Figure 11a and Figure 11b, respectively. As can be seen in the figures, the turn-by-turn data is shown in the blue, where the green envelope is used for the exponential fit for the growth rate. The fit is the orange curve of the form $a + be^{cx}$, where c corresponds to the growth rate. The growth rates in [1/s] are also presented in the figures.

For each first growth observed, the true first growth rate lies between the kicker gain with zero growth and the kicker gain with first growth. To obtain a better estimate of the true threshold growth rate, a linear fit was performed on the kicker gain and growth rate relationship. For every kicker gain within a phase setting, the growth rate was recorded. The relationship between kicker gain and

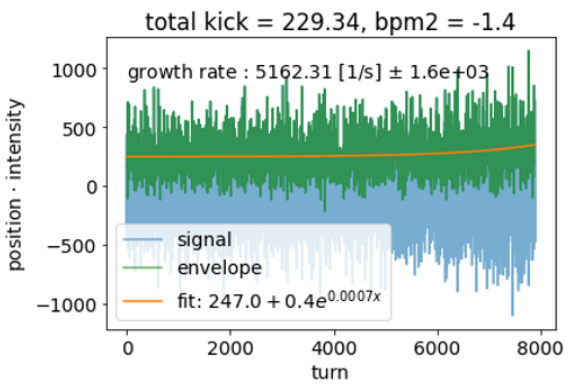

(a) Turn-by-turn beam centroid data at a kicker gain right below the first growth observed.

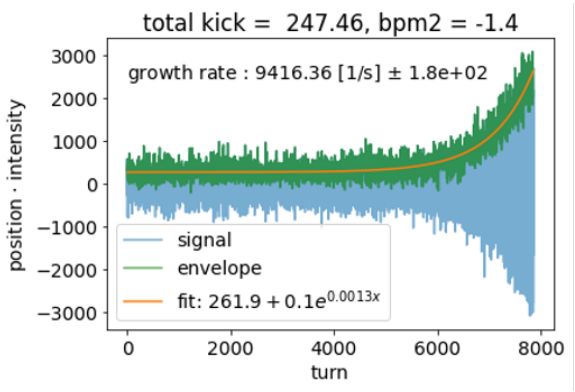

(b) Turn-by-turn beam centroid data at the next kicker gain, right after the first growth.

Figure 11

corresponding growth rate is linear, so a linear fit between these quantities was performed. Looking closely at the linear fit between the no growth and first growth data points, estimates of the first growth rate and the corresponding uncertainty were obtained. An example of the linear relationship between the kicker gain and the growth rate per phase advance can be seen in Figure 12a. The zoomed-in area of the first growth can be seen in Figure 12b. As can be seen from Figure 12b, the region of first growth occurs between the data point with a kick gain of approximately 229 and the point with a kick gain of approximately 247. The turn-by-turn data in the sub-figures of Figure 11 present the growth rates and kicker gains that make up those two data points. The linear fits at the kicker gain right before the first growth are the ones used in propagating this analysis.

It is also important to note that the growth rates for the linear fits were normalized relative to the beam's emittance and the intensity, as the stability diagram size is dependent on those parameters.

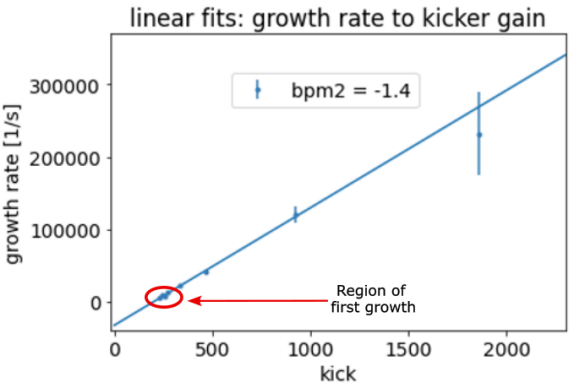

(a) Linear fit between kicker gain and growth rate. The area circled red is the region where the threshold for growth is located.

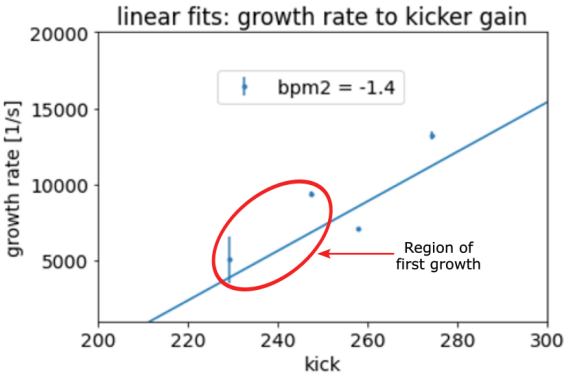

(b) Zoom-in of the same kicker gain and growth rate. The area circled red is between the consecutive kicker gains where the threshold lies.

Figure 12

These linear fits and estimates of first growth rates were performed for each BPM combination. Additionally, this analysis process was performed for both when there were no additional turns before data collection and when there were two additional turns. This enabled data collection for different phase regions. For each turn delay and for each phase a threshold growth rate was obtained and Eq. (3) was used to obtain $Re[\Delta\omega]$ and $Im[\Delta\omega]$. The stability diagrams for the no additional turn and the two additional turn data can be seen below in Figure 13a and Figure 13b, respectivley.

As can be seen in the sub-figures of Figure 13, particularly in Figure 13a, there are some large uncertainties, outliers, and unexpected results in the data. In Figure 13b, there seems to be a systematic

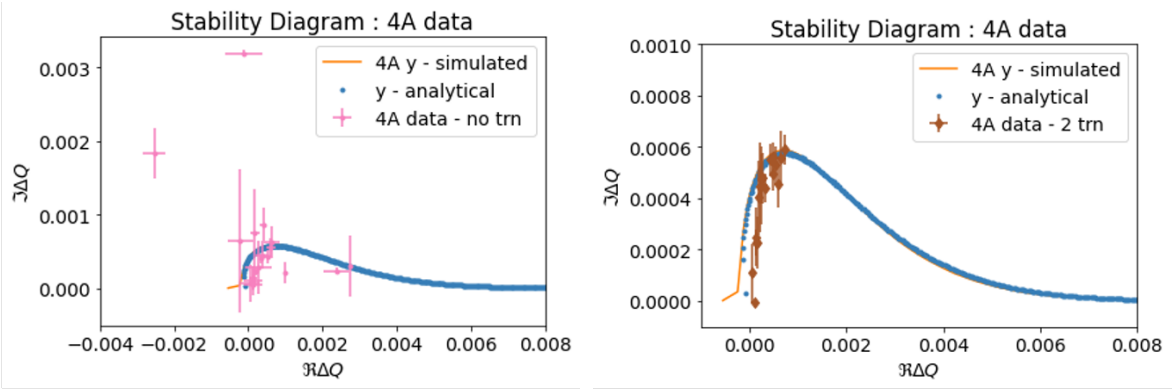

(a) No additional turn delay stability diagram.

(b) Two additional turn delay stability diagram.

Figure 13

rightward shift of the data from the theoretical and simulated stability diagrams. The two data sets with major outliers with poor fits removed are shown together Figure 14.

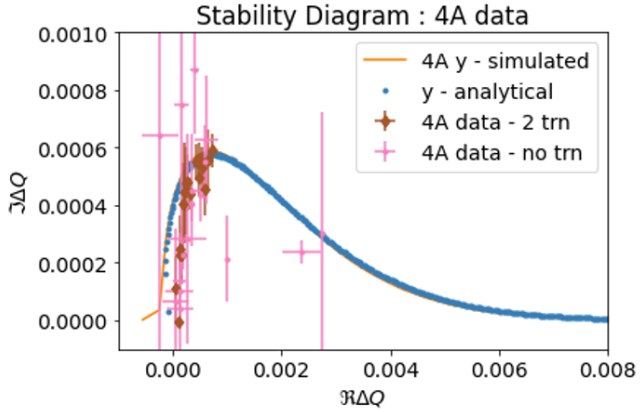

Figure 14: Total stability diagram excluding major outliers.

Again, the major issues seen from these results include large error bars and a systematic rightward shift in the data collected. The error bar sources are mainly from the BTF step size and kick gain step size. The BTF step sizes were so large that the BTF amplitude's Lorentzian fit is visibly off from the data. This can be seen in Figure 10a. This offset in the Lorentzian fit led to shifts in the phase values recorded for each peak amplitude, causing additional uncertainty in the BPM coefficient to phase relationship. The kicker gain steps were also large, such that the step between no growth rate observed for a kicker gain and the first growth rate observed led to large threshold growth rate uncertainties.

One additional thing to consider is that Landau Damping is not the only source of damping in the IOTA ring. Another source of damping to consider is that of synchrotron radiation damping (SRD). The impact of SRD would lead to a shift of the stability diagram. To consider the impact of SRD, $\Delta\omega$ was computed for SRD in IOTA. The resulting shift was $\Delta\omega = 4.4e^{-7} + i \cdot 3.4e^{-7}$. Since the SRD shift in the real and imaginary axes of $\Delta\omega$ are respectively four and three orders of magnitude smaller than the $\Delta\omega$ from Landau Damping, this effect is negligible.

The successes of the NIOLD Run 4 experiment includes the significant increase in quantity of phase measurements for a stability diagram. Instead of three phase measurements on the stability diagram from the LHC proof-of-principle experiment, this experiment had many phase measurements, as seen in Figure 14. Additionally, the experimental data, simulation, and analytical predictions all qualitatively agree, an encouraging step for this measurement method of the stability diagram. This first run for stability diagram analysis was also critical for our understanding of what we need to know

and what we need in data collection. It gave us insight on how we would proceed in future runs and informed us on what data was necessary for measurement of stability diagrams.

6 Next Steps

The next steps for this experiment can be broken up into two seperate sections, next steps for the current set of data and next steps for future data sets.

For the current set of data, one thing we would like to do is investigate the systematic rightward shift in data. This may be due to some systematic issue with phase data collection or analysis processing. Another next step would be to further investigate issues in phase-wrapping. The current results suggest an issue with the calculated phase advance. The beam transfer data is the basis for measuring the system phase and since we have found an issue with the measurements, it needs further study to fully understand and then propagate to the results. This should also be further investigated and better understood before the next data collection. Additionally, a next step would be obtain the beam distribution function from the measured stability diagram. This procedure from stability diagram to beam distribution function is explained in [2]. We would also like to investigate the machine impedance's impact on the stability diagram and compare to the measurements from the LHC.

For future runs, our goals and next steps are further sectioned into those with future electron runs and those with future proton runs.

Next steps and goals for future electron runs include ensuring that we obtain beam size measurements for all the data collected, so we are able to normalize by the emittance. We would also take stability diagram data for various octupole settings to analyze the impact of the octupole strengths on the stability diagram. Additionally, we would obtain more data for tails of the SDs. This is because the tails are essential to obtain an accurate beam distribution function. We would get more data for the tails by taking more measurements at small phases. We would also like to take tighter measurements for the BTFs, so to minimize the phase error. We would also directly measure the amplitude detuning matrix, to compare with calculations. Additionally, in Run 4 we were limited by the antidamper acting and measuring in one plane at a time. In future runs we would like to add the capability to measure in both planes at the same time, even if the antidamper is only acting in one plane at a time.

Next steps for future proton runs include analyzing stability diagrams with the impact of an electron lens in the IOTA ring and investigating Landau Damping in the regime with bunched beams and space charge.

7 Conclusions

In this report we have introduced Landau Damping, an effect that damps collective instabilities in particle accelerators. Landau Damping is often approached via stability diagram theory, where a stability diagram maps out the regions where the beam is damped by Landau Damping and where it is not. We have introduced and proposed a new measurement method to measure stability diagrams in accelerators, which employs an antidamper. We have also presented the data collection process, the data analysis procedure, and the preliminary results. The first results qualitatively agree with the analytical predictions and the simulations. Next steps for the current set of data and ideas and goals for future data were also discussed.

References

[1] S. Antipov. Proof-of-principle direct measurement of landau damping strength at the large hadron collider with an antidamper. *PRL 126*, 2021.

[2] A. Burov. Inverse stability problem in beam dynamics. *PRAB 26*, 2023.

[3] L. Deniau, H. Grote, G. Roy, and F. Schmidt. *The MAD-X Program*, 2022.

[4] N. Eddy, A. Valishev, R. Ainsworth, A. Burov, O. Mohsen, B. Fellenz, and A. Semenov. Iota experiment nonlinear optics: Landau damping (niold). NIOLD Experimental Proposal.

[5] G. Iadarola, R. D. Maria, S. Łopaciuk, A. Abramov, X. Buffat, D. Demetriadou, L. Deniau, P. Hermes, P. Kicsiny, P. Kruyt, A. Latina, L. Mether, K. Paraschou, G. Sterbini, F. F. V. D. Veken, P. Belange, P. Niedermayer, D. D. Croce, T. Pieloni, L. V. Riesen-Haupt, and M. Seidel. Xsuite: An integrated beamphysicssimulationframework. *JACoW HB2023 (2024)*, TUA2I1.

[6] L. Landau. One the vibrations of the electronic plasma. *Journal of Physics*, 1945.

[7] J. Malmberg and C. Wharton. Collisionless damping of electrostatic plasma waves. *PRL 13*, 1964.

[8] L. Palumbo and M. Migliorati. Landau damping in particle accelerators, 2011.

[9] G. Wang. Collective effects and instabilities.